Earth and Planetary Science Letters 311 (2011) 316–327

Contents lists available at SciVerse ScienceDirect

Earth and Planetary Science Letters

journal homepage: www.elsevier.com/locate/epsl

Fault structure, frictional properties and mixed-mode fault slip behavior

Cristiano Collettini [a,b,*], André Niemeijer [c], Cecilia Viti [d], Steven A.F. Smith [b], Chris Marone [e]

[a] Dipartimento di Scienze della Terra Università degli Studi di Perugia, Italy
[b] Istituto Nazionale di Geofisica e Vulcanologia, Roma, Italy
[c] Utrecht University, Faculty of Geosciences, HPT Laboratory, Netherlands
[d] Dipartimento di Scienze della Terra Università di Siena, Italy
[e] Rock and Sediment Mechanics Laboratory Penn State University, USA

ARTICLE INFO

Article history:
Received 23 March 2011
Received in revised form 11 September 2011
Accepted 13 September 2011
Available online 20 October 2011

Editor: P. Shearer

Keywords:
Fault structure
Friction
Fault creep
Earthquakes

ABSTRACT

Recent high-resolution GPS and seismological data reveal that tectonic faults exhibit complex, multi-mode slip behavior including earthquakes, creep events, slow and silent earthquakes, low-frequency events and earthquake afterslip. The physical processes responsible for this range of behavior and the mechanisms that dictate fault slip rate or rupture propagation velocity are poorly understood. One avenue for improving knowledge of these mechanisms involves coupling direct observations of ancient faults exhumed at the Earth's surface with laboratory experiments on the frictional properties of the fault rocks. Here, we show that fault zone structure has an important influence on mixed-mode fault slip behavior. Our field studies depict a complex fault zone structure where foliated horizons surround meter- to decameter-sized lenses of competent material. The foliated rocks are composed of weak mineral phases, possess low frictional strength, and exhibit inherently stable, velocity-strengthening frictional behavior. In contrast, the competent lenses are made of strong minerals, possess high frictional strength, and exhibit potentially unstable, velocity-weakening frictional behavior. Tectonic loading of this heterogeneous fault zone may initially result in fault creep along the weak and frictionally stable foliated horizons. With continued deformation, fault creep will concentrate stress within and around the strong and potentially unstable competent lenses, which may lead to earthquake nucleation. Our studies provide field and mechanical constraints for complex, mixed-mode fault slip behavior ranging from repeating earthquakes to transient slip, episodic slow-slip and creep events.

1. Introduction

A traditional interpretation of tectonic faults is that stress is relieved either as earthquakes resulting from sudden frictional instabilities or by continuous aseismic frictional sliding and fault creep (e.g., Scholz, 1998). In this view, crustal faults have a stable region near the surface (0–3 km), owing to the presence of loosely consolidated material (Marone and Scholz, 1988), and at depth (15–20 km), owing to the onset of viscous deformation of fault rocks with increasing temperature (Brace and Kohlstedt, 1980). Between these depths, within the seismogenic zone, fault slip is envisaged to occur primarily by earthquakes. Frictional processes and the parameters that dictate the stability of frictional sliding are therefore critical for the physics of earthquakes. Several lines of evidence suggest that most seismically active faults are statically strong structures with friction, μ, in the range 0.6–0.85 (e.g. Byerlee, 1978; Scholz, 2000). Geological evidence along seismic faults suggests: 1) that earthquake ruptures are localized within principal slip zones less than a few cm thick, with evidence in some cases of extreme localization within zones mm or less in thickness (e.g., Power and Tullis, 1989; Sibson, 2003) and 2) that dynamic processes may result in a dramatic strength loss from pre-slip, high static friction, to co-seismic, low dynamic friction (e.g. Di Toro et al., 2011; Kitajima et al., 2010). Alternative situations exist in at least some cases, such as the San Andreas in central California, where recent work shows that extreme fault weakness (μ~0.1) occurs within a 3 m wide creeping fault core (Zoback et al., 2010) due to the presence of weak clay minerals (Carpenter et al., 2011).

In the last decade, the development of highly sensitive surface and borehole seismometers and the improvement of geodetic networks have resulted in a re-evaluation of how crustal faults accommodate plate motions (e.g., Peng and Gomberg, 2010). Tectonic faults, in fact, appear to fail by a continuous spectrum of slip modes. Details of aseismic fault creep were first highlighted along the San Andreas fault (e.g. King et al., 1973) and then recognized along other crustal-scale structures (Cashman et al., 2007; Chen et

* Corresponding author at: Dipartimento di Scienze della Terra Università degli Studi di Perugia, Italy.
E-mail address: colle@unipg.it (C. Collettini).

0012-821X/$ – see front matter © 2011 Elsevier B.V. All rights reserved.
doi:10.1016/j.epsl.2011.09.020

al., 2009; Chiaraluce et al., 2007; Hreinsdottir and Bennett, 2009; Waldhauser et al., 2004). Recent work along the central Peru megathrust indicates that 50–70% of the slip budget within the seismogenic zone is accommodated by aseismic slip (Perfettini et al., 2010). Low-frequency earthquakes, episodic non-volcanic tremor, and slow slip events are now recognized as common phenomena along plate boundary faults down-dip of the seismogenic zone (Rubinstein et al., 2010), and also within accretionary prisms (Ito and Obara, 2006). Taken together these observations indicate that slow-slip phenomena occur in many tectonic settings, at different crustal depths and on faults with frictional properties that favor rupture speeds much lower than earthquakes.

In the past years, fault creep interspersed with seismicity, i.e. mixed mode fault slip behavior, has been proposed on the basis of fault zone structure characterization (e.g. Fagereng and Sibson, 2010; Fagereng et al., 2010; Faulkner et al., 2003). Mixed mode fault slip is supported by laboratory experiments on phyllosilicate-bearing fault rock analogs (Niemeijer and Spiers, 2005).

The purpose of this paper is to illuminate the underlying mechanisms and processes of mixed mode fault slip behavior by coupling direct observations of an ancient fault exhumed at Earth's surface with laboratory experiments on the frictional properties of the fault rocks. In particular, we integrate new observations of the structure of the Zuccale fault with fault zone evolution (Smith et al., 2007, 2011) and deformation processes (Collettini and Holdsworth, 2004; Collettini et al., 2009a). We also present new laboratory data and reanalyze existing data (Collettini et al., 2009b) on the velocity dependence and frictional constitutive properties of Zuccale fault rocks. Our laboratory measurements include friction experiments on intact fault rocks sheared in their in situ geometry and experiments on powdered fault gouge. We integrate the suite of laboratory and field observations to illuminate the mechanisms of mixed mode fault slip behavior.

2. Fault zone structure

The Zuccale fault is a regionally-important low-angle normal fault exposed on the isle of Elba in Central Italy. Geological data suggest that the fault has accommodated a total shear displacement of 6–8 km and that the fault zone structure and fault rocks formed at less than 8 km crustal depth (Collettini et al., 2009a). The present day fault structure is the final product of several deformation processes superposed during fault zone exhumation (Smith et al., 2007, 2011). Here, we focus on a series of highly foliated and phyllosilicate-rich fault rocks that represent the basal horizon of the low-angle fault zone. These phyllosilicate-rich fault rocks, formed by dissolution and precipitation processes in carbonate rocks (Collettini et al., 2009a), surround lenses of more competent, non-foliated fault rock materials (Figs. 1 and 2) with observed dimensions ranging from centimeters to tens of meters (though larger lenses may occur). Within the foliated horizons the deformation is continuous and accommodated predominantly by frictional sliding along phyllosilicate lamellae (Collettini et al., 2009a). Frictional sliding is accompanied by the development of foliation-parallel extension veins filled with calcite (Fig. 2b): the crack-and-seal texture of the calcite veins implies cyclic fluid pressure build-up during fault activity (Collettini et al., 2006). The competent lenses are made of intact carbonates, which are not significantly affected by dissolution processes (Fig. 2a), and mafic materials that have been sheared off the wall rocks and incorporated into the fault zone (Fig. 2c–e). In the competent lenses, part of the deformation is localized along discrete minor faults (Fig. 2a and c) with associated cataclastic fault rocks: the presence of calcite veins suggests fluid-driven brittle processes (Fig. 2b and d). In some outcrops, it is possible to observe minor faults that cross both the competent lenses and part of the foliated horizons (Fig. 2e). Minor footwall normal faults, with meter-scale displacements, merge into the base of the low-angle fault zone (Fig. 1 and Smith et al., 2007). Field evidence indicates that low-angle slip within the foliated, phyllosilicate-rich horizons containing the competent lenses occurred broadly synchronously with slip along the minor footwall normal faults. The foliated and phyllosilicate-rich horizons presumably formed continuous layers in the early stages of fault activity, but during fault zone evolution, growth of the footwall normal faults led to thickening of the phyllonitic fault core and eventual dismemberment of the phyllonites in to a series of isolated fault rock units: the present day thickness of the phyllonites is in the range 0–8 m (details of fault slip history and fault zone evolution are presented in Smith et al., 2007; 2011).

Our field studies document a fault zone structure characterized by a mixture of materials and fault slip behavior. To quantify these observations, we investigated the frictional strength and slip stability of the fault rocks via detailed laboratory experiments.

3. Frictional properties of the fault rocks

3.1. Frictional strength

We selected fault rocks representative of both the foliated phyllosilicate-rich horizons, zones 1 and 2 (Figs. 1 and 2 and Table 1),

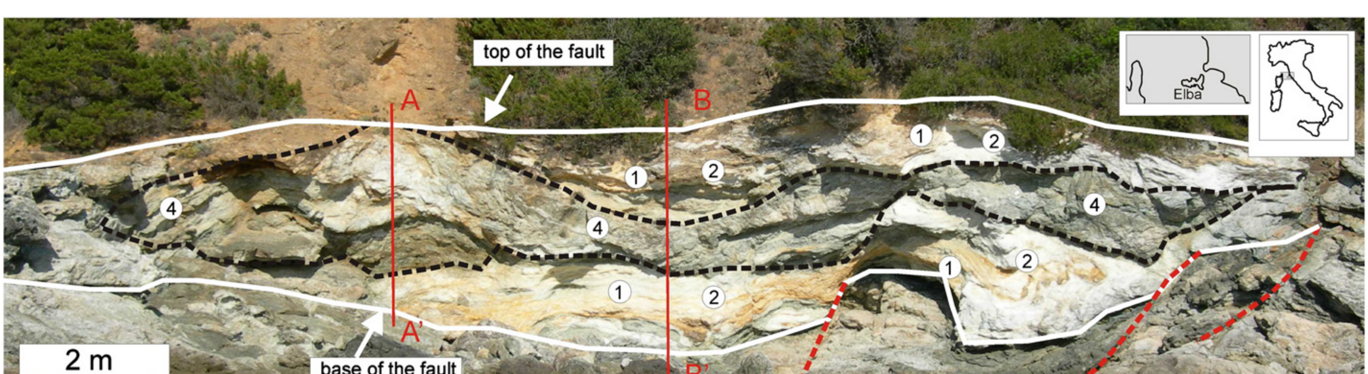

Fig. 1. Fault zone structure of the Zuccale fault, Isle of Elba (Central Italy). Foliated and phyllosilicate-rich horizons (zones 1 and 2) surround stronger lenses of mafic materials (zone 4). Red dashed lines mark the location of brittle faults. A–A′ and B–B′ are transects used to infer strain rate gradients along the fault zone (see Discussion).

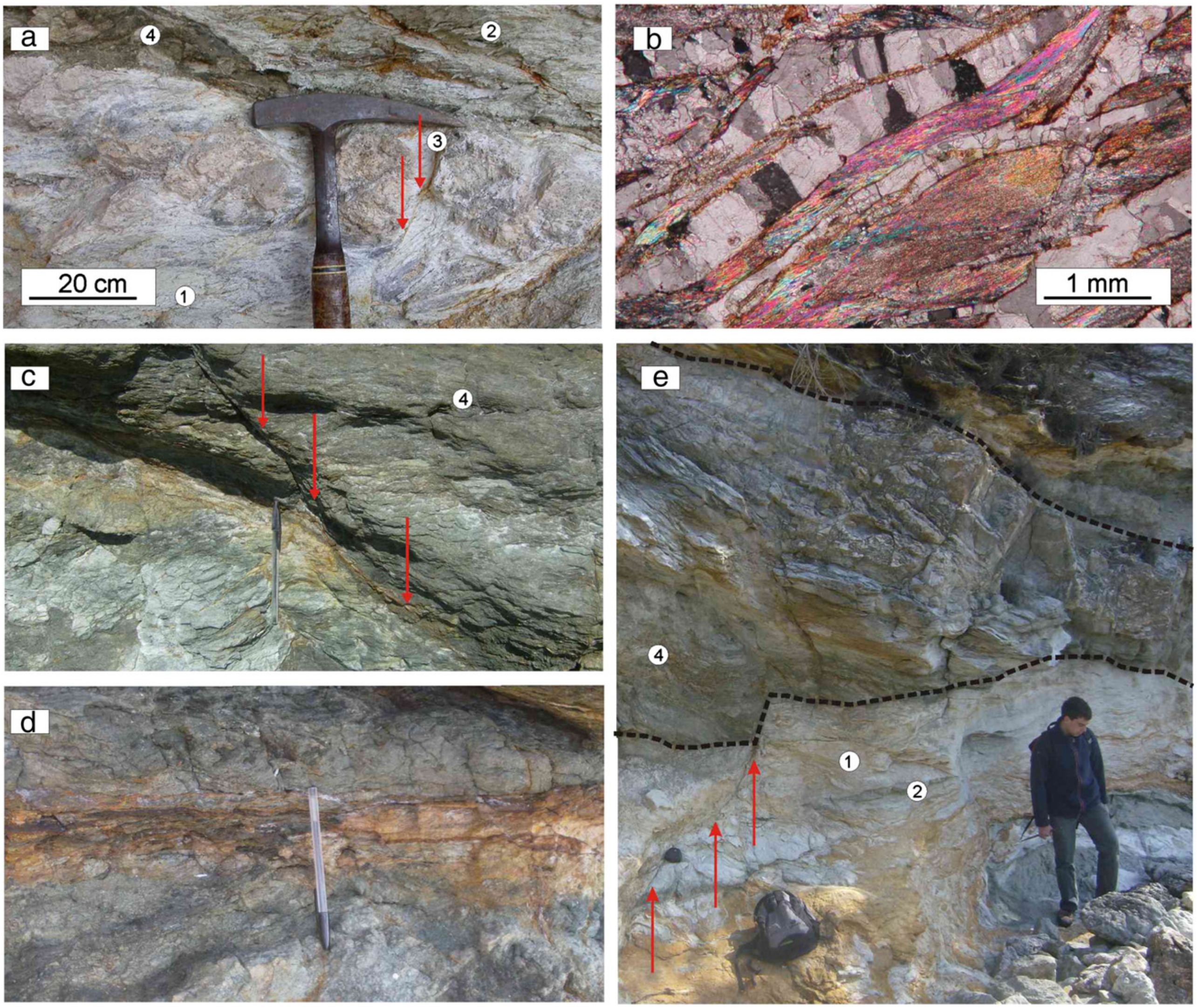

Fig. 2. Details of the fault zone structure. a) Foliated and phyllosilicate-rich horizons (zones 1 and 2) surrounding stronger lenses of carbonate (zone 3) and mafic material (zone 4): the red arrows mark a brittle fault within carbonates. b) Micrograph of the foliated and phyllosilicate-rich microstructure (pink–yellow birefringence colors) developed contemporaneously with extensional veins (pink-gray birefringence colors). c) Localized brittle fault (marked by red arrows) within a competent lens of mafic material (zone 4). The fault is filled with calcite veins suggesting fluid driven brittle processes: details are presented in panel d). e) Minor fault, marked by red arrows, that crosses both a competent lens (zone 4) and the foliated horizons (zones 1 and 2).

and the competent lenses, zones 3 and 4 (Figs. 1 and 2 and Table 1). In zones 1 and 2 the microstructure involves an interconnected and phyllosilicate-rich network (smectite, talc and chlorite) surrounding clasts of stronger mineral phases (calcite and tremolite). Zone 2 is characterized by a higher content of tremolite (Table 1), which gives it a more greenish color compared to zone 1 which is whitish in color. The mineralogy of zone 3 is similar to zone 2, but the deformation is localized along small brittle faults

Table 1
Experimental details and mineral composition of the tested rocks. Sampling points for rocks representative of both the foliated horizons (zones 1 and 2) and the competent lenses (zones 3 and 4) are shown in Figs. 1 and 2.

Exp.	Sample	Normal stress (MPa)	Sliding velocities (μm/s)	Mineralogy
P2041	4 powder	10, 20, 35, 50	1, 3, 10, 30, 100, 300	Bt 33, Chl 12, Hbl 55
P2044	4 powder	75, 100, 150	1, 3, 10, 30, 100, 300	Bt 33, Chl 12, Hbl 55
P2048	1 foliated	10, 20, 35, 50	1, 3, 10, 30, 100, 300	Cal 39, Tlc 14, Sm 20, Tr 26, Chl 1
P2052	1 foliated	75, 100, 150	1, 3, 10, 30, 100, 300	Cal 39, Tlc 14, Sm 20, Tr 26, Chl 1
P2053	2 foliated	75, 100, 150	1, 3, 10, 30, 100, 300	Cal 43, tlc 6, Sm 14, Tr 36, Chl 1
P2054	2 foliated	10, 20, 35, 50	1, 3, 10, 30, 100, 300	Cal 43, tlc 6, Sm 14, Tr 36, Chl 1
P2056	3 powder	10, 20, 35, 50	1, 3, 10, 30, 100, 300	Cal 43, tlc 6, Sm 14, Tr 36, Chl 1
P2066	3 powder	75, 100, 150	1, 3, 10, 30, 100, 300	Cal 43, tlc 6, Sm 14, Tr 36, Chl 1
P2057	2 foliated/wet	10, 20, 35, 50	1, 3, 10, 30, 100, 300	Cal 43, tlc 6, Sm 14, Tr 36, Chl 1

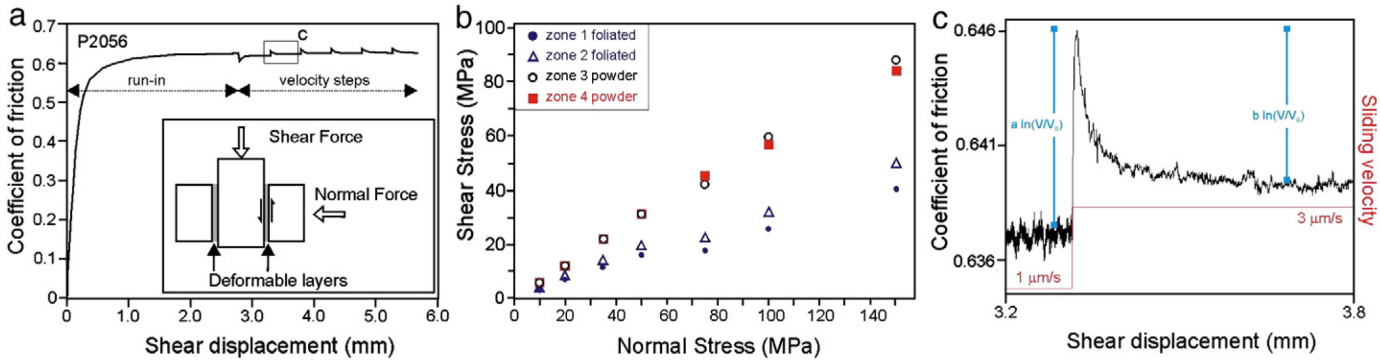

Fig. 3. Laboratory friction data. a) Coefficient of friction μ versus shear displacement for a representative experiment at a normal stress of 20 MPa. The experiment starts with a run-in phase at constant sliding velocity of 10 μm/s and five velocity steps from 1–300 μm/s. b) Steady state shear stress measured during frictional sliding at the end of the run-in phase, plotted as a function of normal stress. Data for the foliated intact rocks plot along lines with slopes μ = 0.25 and μ = 0.31 for samples 1 and 2 respectively. Data for powdered rocks from the strong lenses plot along lines with slopes μ = 0.55 and μ = 0.62 for samples 3 and 4 respectively. c) Detail of panel a showing the evolution in friction for a velocity step from 1 to 3 μm/s.

affected by cataclastic processes (Fig. 2a). Zone 4 is derived from a mafic protolith and is composed of hornblende, biotite and chlorite. To take into account the role of foliation in frictional properties we conducted friction experiments on: a) intact fault rocks of the foliated samples sheared under their in situ geometry, i.e. zones 1 and 2 (Collettini et al., 2009b) and 2) powders prepared by crushing fault rock materials from the competent lenses, i.e. zones 3 and 4. The competent lenses are cross-cut by minor faults characterized by cataclasis and grain size reduction (Fig. 2a, c and e), suggesting that experiments on both powders rather than on solid samples, are more appropriate to investigate the frictional properties of these fault rocks. Powders were obtained by crushing and sieving (150 μm) fault rocks from the competent lenses. For experiments on intact, foliated fault rocks we used natural samples 0.8–1.2 cm thick and 5 × 5 cm in area and followed procedures documented in Collettini et al. (2009b) and Ikari et al. (2011).

Frictional sliding experiments were conducted in the double direct shear configuration (Fig. 3a inset) at room temperature and humidity (~25 °C and ~25% relative humidity), over a range of normal stresses from 10 to 150 MPa. The foliated fault rocks from zones 1 and 2 exhibit sliding friction coefficients in the range 0.25–0.31 (Collettini et al., 2009b), implying that the phyllosilicate-rich fault rock horizons are weak (Fig. 3b). In contrast, fault rocks from the competent lenses of zones 3 and 4 exhibit sliding friction coefficients in the range 0.55–0.62 (Fig. 3b), suggesting that the competent lenses are strong fault portions.

3.2. Constitutive modeling for friction parameters

In order to investigate possible modes of fault slip-behavior, we measured the velocity dependence of sliding friction of the fault rocks. For all samples, after a 'run-in' phase (Fig. 3a) at a constant sliding velocity of 10 μm/s, we applied a velocity-stepping sequence consisting of 5 steps from 1–300 μm/s, with displacements during individual steps of 500 μm. Velocity step tests (Fig. 3c) involved imposing step changes in sliding velocity from V_0 to V (e.g. Dieterich, 1979; Marone, 1998; Ruina, 1983; Scholz, 1998). For each velocity step, the instantaneous change in friction coefficient scales as the friction parameter $a\ \ln(V/V_0)$, and is always of the same sign as the velocity change. The decay to a new steady state value of sliding friction scales as the friction parameter $b\ln(V/V_0)$, and is usually of the opposite sign of the velocity change. a and b are empirical constants (unitless) defined as the direct effect and the evolution effect respectively (e.g. Ruina, 1983). Frictional velocity dependence is defined as:

$$(a{-}b) = \frac{\Delta\mu_{ss}}{\ln(V/V_0)} \tag{1}$$

where $\Delta\mu_{ss}$ is the change in the steady state coefficient of friction due to a change in sliding velocity from V_0 to V. Positive values of $(a-b)$ indicate velocity-strengthening frictional behavior which results in stable fault sliding and is associated with aseismic fault creep. Negative values of $(a-b)$ indicate velocity-weakening frictional behavior, which is a prerequisite for unstable, stick–slip behavior associated with earthquake nucleation (e.g. Dieterich and Kilgore, 1994; Marone, 1998; Scholz, 1998).

We modeled friction data from velocity-step tests using the rate and state variable friction equations (Fig. 4 and Ruina, 1983; Saffer and Marone, 2003):

$$\mu = \mu_0 + a\ln\left(\frac{V}{V_0}\right) + b\ln\left(\frac{V_0\theta}{d_c}\right) \tag{2}$$

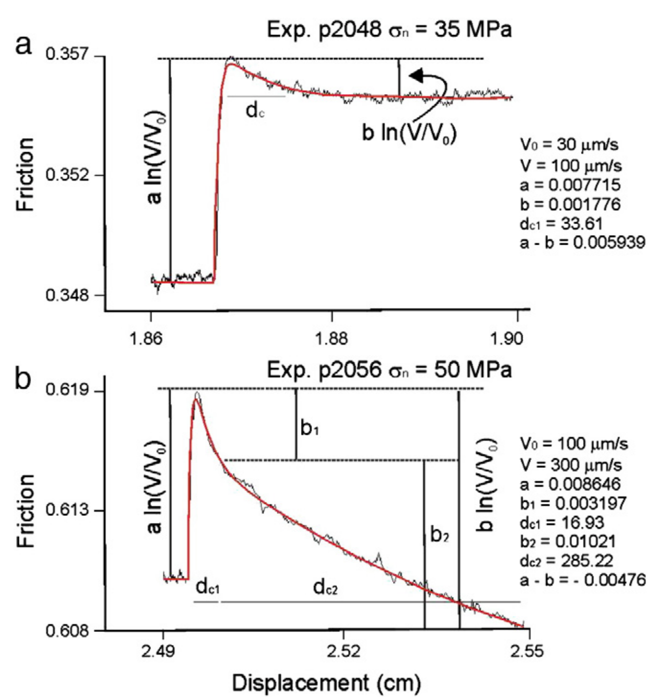

Fig. 4. a) Modeling results for constitutive friction parameters a, b, d_c and $a-b$ for experiment p2048, zone 1 foliated. b) For experiment on zones 3 powders, the frictional decay is better represented by two evolution parameters b_1 and b_2 (where $b = b_1 + b_2$) and two associated critical slip distances d_{c1} and d_{c2}. The black line is evolution of friction upon a velocity step, the red line is the modeling result. Friction parameters are presented in Appendices A and B.

$$\frac{d\theta}{dt} = \left(1 - \frac{V\theta}{d_c}\right), \text{Dieterich evolution equation} \quad (3)$$

where μ_0 is a reference friction value, θ is a state variable and d_c is the critical slip distance. The state variable is inferred to be the average lifetime of asperity contacts that control friction, and the critical slip distance is the displacement over which the population of asperity contacts are renewed (Marone and Kilgore, 1993; Scholz, 1998). The interaction of the sample with its elastic surroundings is incorporated according to the equation:

$$\frac{d\mu}{dt} = k\left(V_{lp} - V\right) \quad (4)$$

where k is the stiffness of the fault surroundings (in the laboratory this represents the testing apparatus and the sample blocks), normalized by the normal stress ($k = \sim 3 \times 10^{-3}\ \mu m^{-1}$ at 25 MPa normal stress), V_{lp} is the load point velocity, and V is the true slip velocity. We solve Eqs. (2) and (3) simultaneously, with Eq. (1) as a constraint, using a fifth-order Runge–Kutta method. The constitutive parameters (presented in Appendices A and B) are obtained as solutions to a nonlinear inverse problem using an iterative least squares method (e.g., Blanpied et al., 1998; Reinen and Weeks, 1993; Saffer and Marone, 2003). For some samples, zone 3, the decay of friction to a new steady state condition following a velocity step is better modeled using two state variables, leading to two evolution parameters, b_1 and b_2 ($b = b_1 + b_2$) associated with two critical slip distances, d_{c1} and d_{c2} respectively. Fig. 4 shows examples of one- and two-state variable behavior.

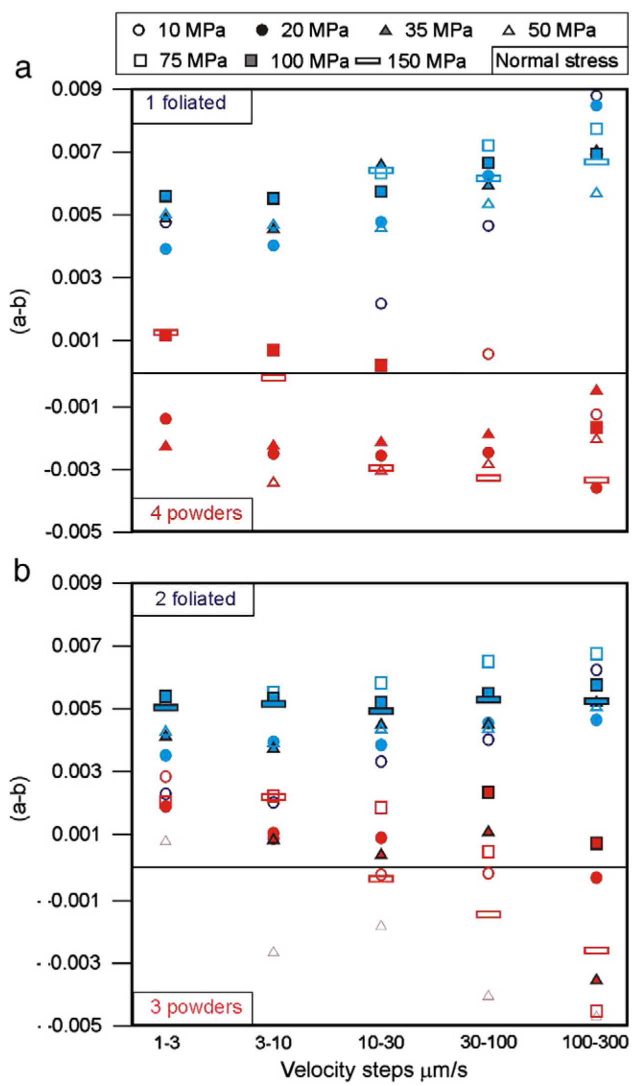

Fig. 5. Frictional velocity dependence $(a-b)$ as a function of normal stress and sliding velocities. The foliated samples (zones 1 and 2, see location in Figs. 1 and 2) are characterized by velocity-strengthening frictional behavior, positive $(a-b)$. The powders (zones 3 and 4, see location in Fig. 1 and 2) evolve from velocity strengthening, to velocity-weakening with increasing sliding velocity.

3.3. Friction parameters for foliated horizons and microstructures

In our experiments the intact foliated rocks exhibit positive $(a-b)$ values for the entire range of normal stresses (10–150 MPa) and sliding velocities (Fig. 5). The degree of velocity strengthening increases with sliding velocity, with $(a-b)$ values up to 0.009 and 0.007 for zones 1 and 2 respectively (Fig. 5a and b). Analysis of the friction parameters *a* and *b* shows that the foliated rocks are characterized by a distinct direct effect that is independent of the applied normal stress and that increases with increasing sliding velocity (Fig. 6), whereas the evolution effect is very small, in some cases close to zero. In these samples, deformation is mainly accommodated within the phyllosilicate-rich horizons by foliation-parallel sliding surfaces, interlayer delaminations and micro-folds (Fig. 7a–d), whereas cataclasis and grain size reduction is rare. These microstructural observations are consistent with the observed low *b* values, confirming the concept of “contact saturation”, in which mineral surfaces are in complete contact and thus the real area of contact does not evolve when the velocity is perturbed (e.g. Ikari et al., 2009; Niemeijer et al., 2010; Saffer and Marone, 2003).

3.4. Friction parameters for the competent lenses and microstructures

For the fault rocks derived from the competent lenses, we observe that zone 3 shows an evolution from velocity strengthening, $(a-b)$ ~0.003, to velocity-weakening behavior, $(a-b) \sim -0.005$, with increasing sliding velocity (Fig. 5b). Zone 4 shows a similar evolution towards velocity-weakening with increasing sliding velocity, but some velocity-weakening is also measured at low sliding velocities (Fig. 5a). For both zones 3 and 4 the friction parameters *a* and *b* are independent of the applied normal stress and they increase with increasing sliding velocity (Fig. 6). A distinct evolution effect is documented at high sliding velocities and in particular for zone 4 (Fig. 6). The microstructure of the powdered materials from the fault lenses is generally characterized by two fine-grained slipping zones located near the boundaries of the shear zone and a central zone not affected by grain size reduction (e.g. Fig. 7e–i). Microstructural observations suggest that deformation is mainly accommodated by cataclasis with grain size reduction and localization along B, R1 and Y shear planes (e.g. Beeler et al., 1996; Cowan et al., 2003; Logan, 1978; Marone, 1998).

4. Discussion

The structure of the Zuccale fault zone seems to be quite similar to other mature, phyllosilicate-rich fault zones (e.g. Gueydan et al., 2003; Holdsworth, 2004; Moore and Rymer, 2007; Wintsch et al., 1995). For example, the Carboneras fault zone in Spain is a c.1 km wide strike-slip fault zone composed of continuous strands of foliated phyllosilicate-rich horizons that bound lenses of more competent materials cross-cut by discrete brittle faults (Faulkner et al., 2003). A similar fault zone structure is proposed for the Median Tectonic Line in Japan (Jefferies et al., 2006; Wibberley and Shimamoto, 2003). Additionally, field studies of exhumed subduction-related shear zones depict a thick fault zone in which overall shearing is accommodated by foliated horizons that surround rock lenses with different mechanical properties

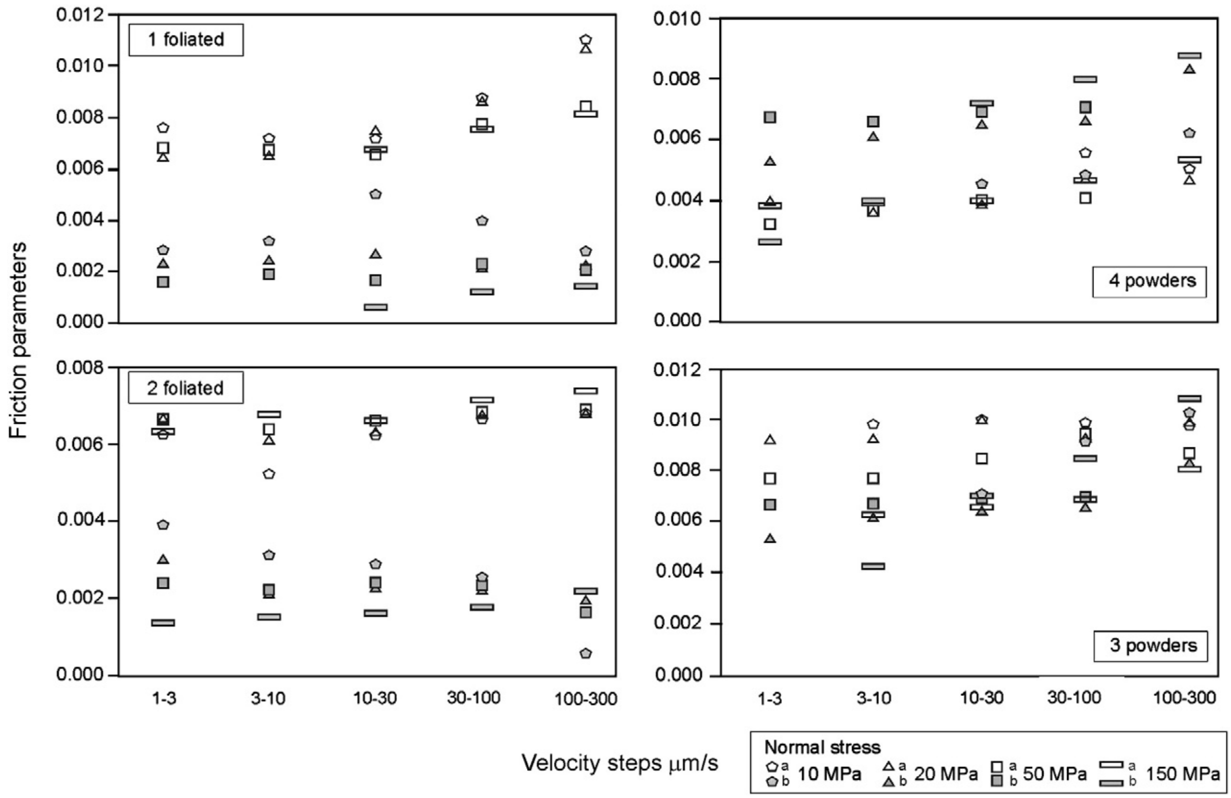

Fig. 6. Friction parameters *a* and *b* of the tested rocks as a function of normal stress and sliding velocities.

(Fagereng and Sibson, 2010; Vannucchi et al., 2007). This picture of fault zone structure, characterized by distributed deformation within a thick phyllosilicate-rich shear zone, differs from the typical geological interpretation of seismic faults, where deformation is localized within thin principal slip surfaces (Chester and Chester, 1998; Sibson, 2003). Instead, in weak fault zones the deformation is distributed within a thick shear zone composed of varied fault rocks with different frictional properties.

Here we propose a model for slip behavior of heterogeneous fault zones, like the Zuccale fault, that is consistent with our laboratory observations. In particular, the model is based on two end members: the weak foliated horizons (zones 1 and 2) and the strong competent lenses (zones 3 and 4). To mimic frictional sliding along the foliated and phyllosilicate-rich horizons, we used the frictional properties obtained from solid foliated wafers from zones 1 and 2. Because deformation in the competent lenses is characterized by slip on small faults affected by cataclastic processes (e.g. Fig. 2a, c and e), we use results from our experiments on powders from zones 3 and 4 to represent these. At the same time, it is worth noting that a contribution to deformation is likely to come from pressure solution creep (Bos and Spiers, 2002; Chester, 1995; Gratier et al., 2009; Niemeijer and Spiers, 2007; Niemeijer et al., 2009; Smith et al., 2011).

Our experiments have been conducted on dry samples and at room temperature: in the following we discuss the applicability of our results to fluid saturated faults at temperatures expected for the shallow crust. For the phyllosilicate-rich horizons, our experiments conducted on wet samples sheared in their in-situ geometry show that the presence of fluids weakens the fault rock: we observe a decrease in friction of about 0.2 for the same lithology, but the velocity-strengthening behavior does not change with the added fluid (Fig. 8). We note only a more pronounced evolution effect on fluid-saturated samples in comparison to dry ones (Fig. 8). Because recent experimental studies have shown that phyllosilicates like talc and smectite remain weak and velocity-strengthening with increasing temperature (Moore and Lockner, 2007, 2008), we infer that our foliated fault rocks, where slip is accommodated by the phyllosilicate foliation (e.g. Fig. 7a–d), will remain weak and velocity-strengthening with increasing temperature. For the strong competent lenses very few frictional data are available on powders composed of calcite, tremolite and phyllosilicates (zone 3) or amphibole and phyllosilicates (zone 4). Experiments conducted on water-saturated calcite powders, at lower displacements (<2.5 mm) and sliding velocities (0.12–1.22 μm/s) compared to our experiments, show that with increasing temperature calcite evolves from velocity strengthening between 25–50 °C, to velocity-weakening at 150 °C (Verberne et al., 2010). This suggests that, in addition to the increase in sliding velocity and shear localization as documented by our data, an increase in temperature can promote frictional instabilities in carbonate-rich rocks. Preliminary data on powders collected from the Zuccale fault with a mineralogical composition similar to zones 3 and 4 show that an increase in fluid pressure and temperature favor frictional instabilities (Niemeijer et al., 2011).

Following a discussion of the applicability of our laboratory results to fluid-rich faults in the shallow crust, we proceed with illustrating the details of the model. During tectonic loading, the shear stress rises until it reaches the frictional strength of the weak, foliated horizons (Fig. 9a), and the fault will begin to slip (Fig. 9b point 1). Because the weak regions exhibit velocity-strengthening frictional behavior (e.g. Figs. 9c and 5), the fault should undergo stable sliding and aseismic fault creep during this phase of slip. With continued shear, however, the tectonic stress may increase due to a combination of geometric factors (related to interaction between weak and strong regions within the fault zone) and variations in fluid pressure within the fault system (see discussion below). When the shear stress reaches the frictional strength of the strong lenses (Fig. 9b point 2),

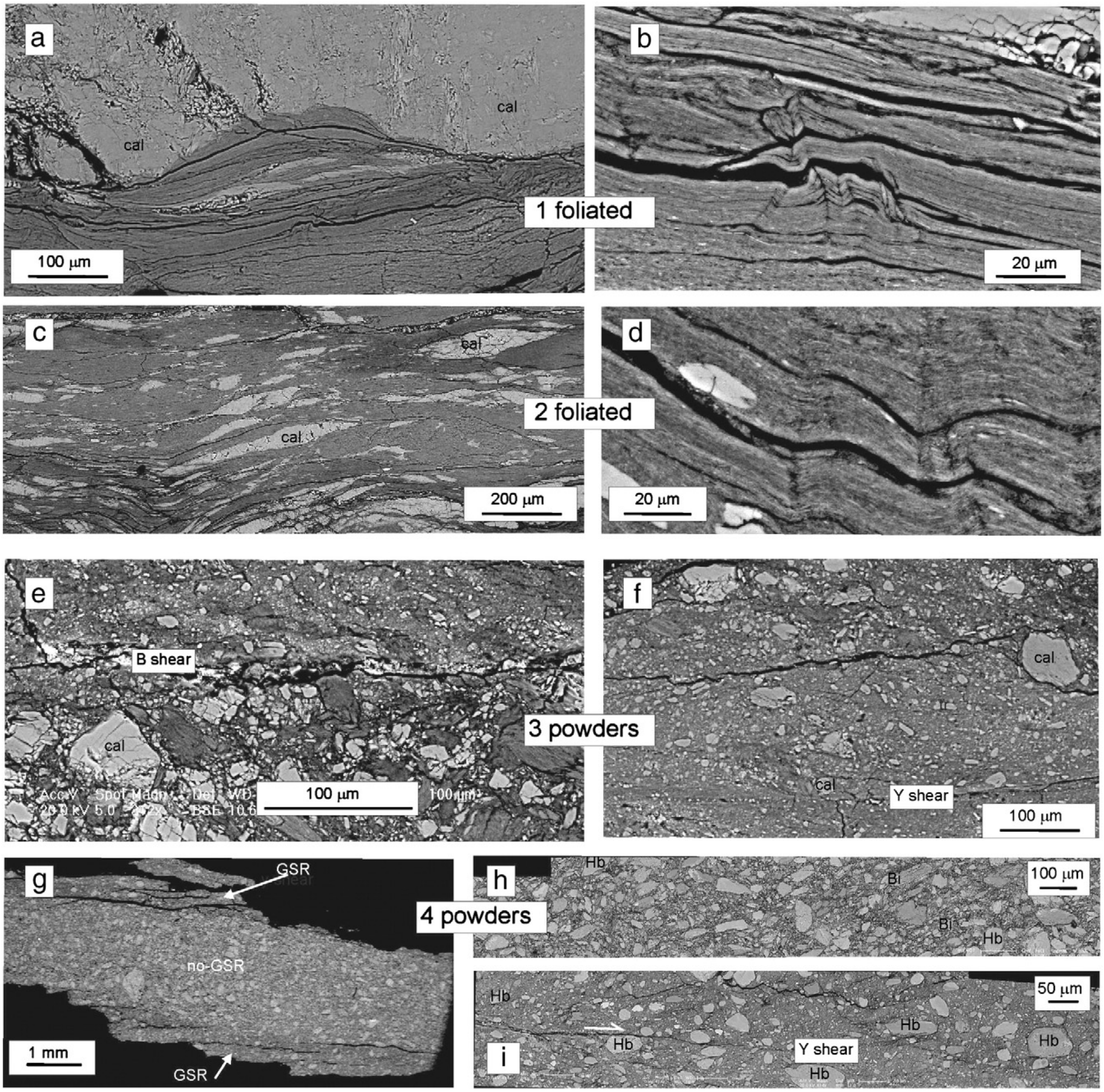

Fig. 7. a–d) Deformation processes in the foliated samples are represented by foliation parallel sliding surfaces, interlayer delaminations (a, b and d) and micro-folds (b and d). a) Calcite clasts not affected by fracturing and foliation-parallel sliding surfaces within the phyllosilicate-rich fault portion. b) Micro-fold and interlayer delaminations within the talc and smectite rich microstructure. c) Calcite sigmoids folded within the phyllosilicate-rich horizons. d) Details of micro-folds and interlayer delaminations within the phyllosilicate-rich microstructure. e–i): The powder experiments are characterized by a central zone with little grain size reduction and two zones located near the boundaries of the shear zone that indicate significant grain size reduction and shear localization along fault parallel shear planes (so called B and Y shear planes). e) a B shear plane separating two fault portions characterized by different amount of grain size reduction. f) In the fault portion affected by grain size reduction, deformation is localized along Y shear planes. g) Fault rock microstructure highlighting two boundary zones characterized by grain size reduction, GSR, and a central zone not affected by this process, no-GSR. Details of the no-GSR h) and GSR i) zones. In the latter and Y shear plane cuts an hornblende clast. All the microstructures are for experiments after a total shear displacement of ~25 mm at normal stress of 50 MPa. Cal = calcite; Hb = hornblende; Bi = biotite.

fractures and/or a frictional instability in the strong lenses may nucleate. The localization of deformation along discrete brittle surfaces observed along the strong lenses (Fig. 2) and the velocity-weakening frictional behavior of the material from the strong lenses (e.g. Figs. 9d and 5) suggest that fault slip may become unstable, leading to seismic rupture.

Fault creep within the phyllosilicate-rich horizons may also increase shear stress on the minor faults that merge into the base of the main fault zone (e.g. Fig. 1), which would tend to promote seismic rupture nucleation along these structures. Both the strong lenses and the minor normal faults may remain in broadly the same location for long time periods, extending over several seismic cycles. This could result in repeated rupture nucleation at a given position on the fault (e.g. repeating earthquakes, Chen et al., 2009; Chiaraluce et al., 2007; Waldhauser et al., 2004).

The Zuccale fault is an ancient and exhumed low-angle normal fault within the Apenninic extensional system. In the currently active area of the Apennines, the Altotiberina low-angle normal fault is accommodating

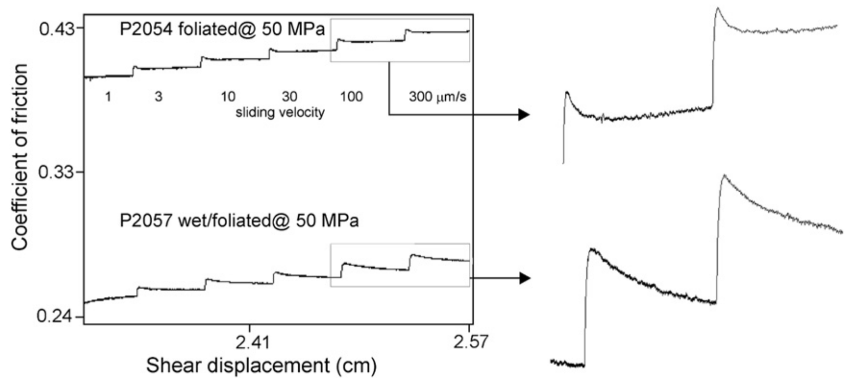

Fig. 8. Comparison of frictional properties of solid foliated samples dry (P2054) and wet (P2057) at 50 MPa of normal stress during velocity steps. For the same mineralogy (cf. Table 1) friction decreases from dry to wet but the velocity-strengthening behavior is confirmed.

extension by microseismicity and aseismic creep at rates of ≈2.5 mm/yr (Chiaraluce et al., 2007; Hreinsdottir and Bennett, 2009). Along this fault, clusters of seismicity have been identified including small, repeating earthquakes with M_L from 0.4 to 1.6 and rupture dimension of radius ~10–70 m (Chiaraluce et al., 2007). We note that Zuccale fault (Fig. 1) contains decameter-sized lenses of competent material, which is consistent with the dimensions of the repeating earthquakes recorded along the Altotiberina fault. Larger earthquakes could be induced by larger lenses not documented in the exposed outcrops, clusters of small competent lenses along the fault zone (e.g. Fagereng, 2011), and/or rupture propagation from the strong competent lenses into the foliated horizons which might become velocity-weakening at higher sliding velocities (Boutareaud et al., 2008; Niemeijer and Spiers, 2007).

Recently by using a dense seismic array in South African mines, it has been shown that mining-induced earthquakes follow the Gutenberg–Richter relation at moment magnitude $M_W = -1.3$ (Boettcher et al., 2009), implying a nucleation zone size for these earthquakes smaller than 25 cm (Boettcher et al., 2009; Fagereng, 2011). These nucleation zones, or asperities, are of the same length scale as numerous competent lenses documented by our field and laboratory data.

In the following, we discuss factors that might promote the episodic occurrence of failure within the strong and competent lenses. One possible cause of repeated failure is geometric factors that result from competency contrast between the strong lenses and the weak and phyllosilicate-rich horizons. Material heterogeneity results in differences in strain rate and finite strain magnitude between

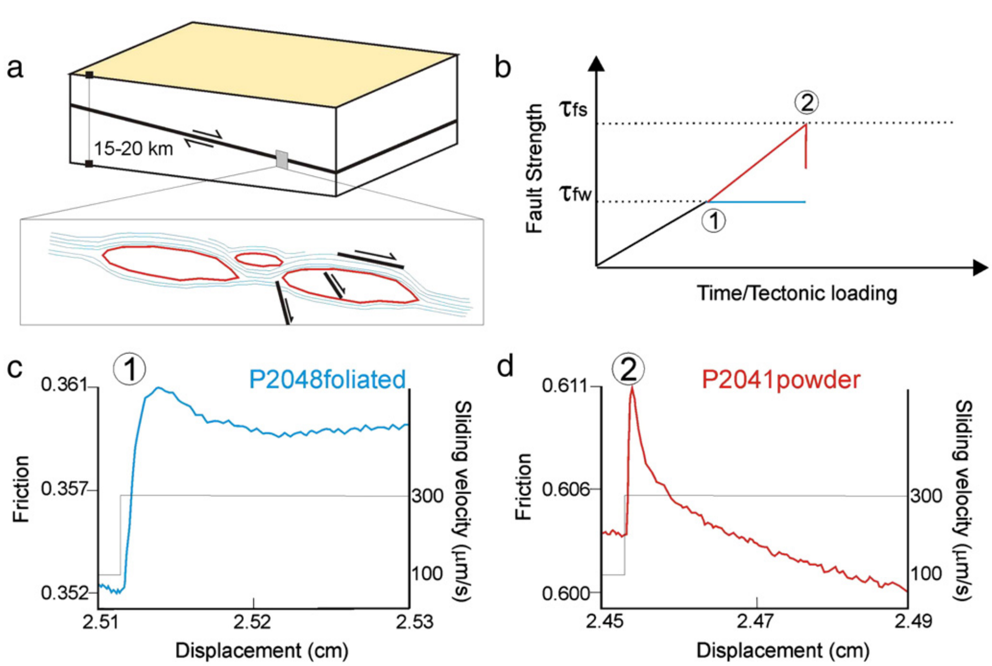

Fig. 9. Proposed model for mixed mode fault slip behavior. a) Schematic representation of a phyllosilicate-rich fault, as inferred for the Zuccale fault. b) Friction and velocity dependence of friction for a heterogeneous fault zone structure. Weak and foliated, phyllosilicate-rich strands (blue) vs. competent and strong fault lenses (red). τ_{fw} shear strength of the phyllosilicate-rich foliation, τ_{fs} shear strength of the strong lenses. c) and d) Details of velocity steps for experiments p2048 solid foliated sample and p2041 powders.

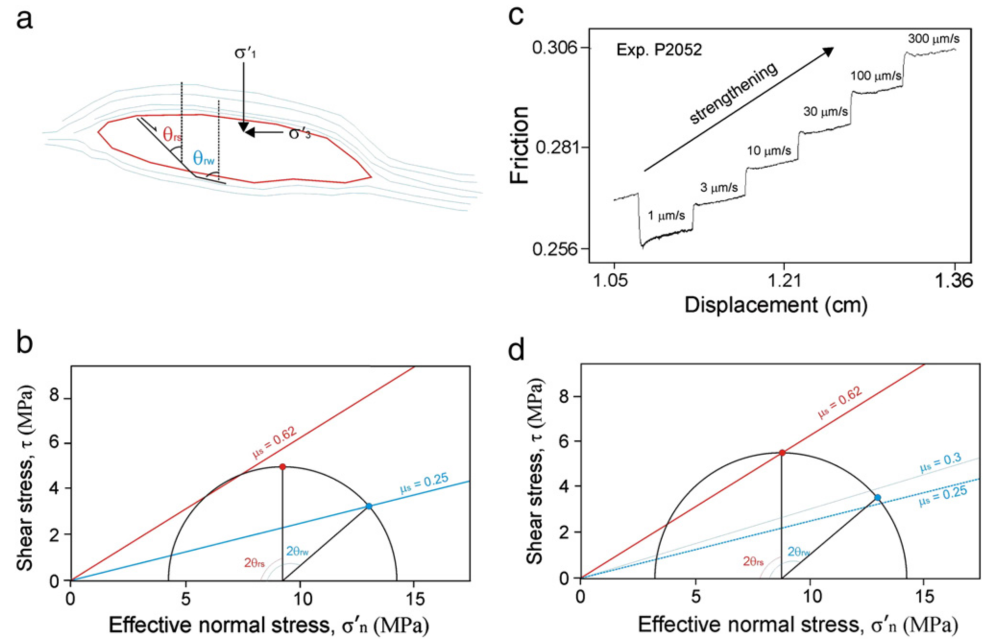

Fig. 10. a) Schematic drawing of fault geometry. θ_{rs} and θ_{rw} are the reactivation angles for re-shear of strong and weak fault portions respectively. Note that in extensional environment the reactivation angle is the complementary of fault dip. b) Mohr diagram illustrating condition for slip along the phyllosilicate-rich fault portions. c) Shear strengthening with increasing sliding velocity, experiment P2052 from zone 1. d) Mohr diagram accounting for restrengthening (dashed blue line) and illustrating the condition for reactivation of faults within the competent lenses induced by an increase of differential stress of 1 MPa from the stress condition reported in b).

competency domains that must be accommodated along the domain boundaries (e.g. Goodwin and Tikoff, 2002). These incompatibilities, if small, can be accommodated by domain-boundary deformation mechanisms, but if sufficiently large, they produce mechanical instabilities resulting in the nucleation of faults (Fagereng and Sibson, 2010; Goodwin and Tikoff, 2002). We start by considering a slip rate of 2.5 mm/yr, v, (the slip rate of the Altotiberina fault measured by Hreinsdottir and Bennett, 2009) and noting that the deformation is accommodated by homogeneous simple shear along the weak and phyllosilicate-rich horizons (thickness, w). Then by considering the distribution of competent vs. incompetent material within the fault zone, it is possible to estimate the fluctuation in strain rate, $\dot{\gamma}=v/w$. For example, along transect A–A′ (Fig. 1) the thickness of the weak material is 0.5 m and the resulting strain rate is $\dot{\gamma}=1.6*10^{-10}\,s^{-1}$. Along transect B–B′ there are two weak portions with a thickness of 2.5 m each, with $\dot{}\gamma\,1.6*10^{-11}\,s^{-1}$; lower strain rates can be related to thicker portions of phyllonites. In general, variable strain rates are strongly related to the amount of competent vs. incompetent materials within the shear zone (e.g. Fagereng and Sibson, 2010). The proposed analysis shows that the value of $\dot{\gamma}$ varies within heterogeneous fault zones like the Zuccale fault, suggesting that strain rate magnitudes can be sufficiently large to produce mechanical instabilities and faulting within the competent lenses.

Another cause that might trigger failure within the competent lenses is fluid pressure within the fault system. Here we investigate with Mohr circles the stress conditions required to induce slip within the weak phyllosilicate-rich horizons and reactivation of small faults within the strong lenses. We study this 2D mechanical problem (for a 3D analysis, see Collettini and Trippetta, 2007; Lisle and Srivastava, 2004; Morris et al., 1996), where the fault planes lie parallel to the σ_2 direction (e.g. Sibson, 1985), at 5 km of crustal depth, a representative exhumation depth of the investigated fault rocks (Collettini et al., 2009a). We assume an extensional environment characterized by a vertical, effective maximum principal stress, σ'_1 (Collettini and Holdsworth, 2004), and low differential stress $(\sigma'_1–\sigma'_3)=10$ MPa. We note that similar low values of differential stress have been inferred for frictional reactivation of phyllosilicate-rich faults oriented at high angles to the maximum compressive stress (Fagereng et al., 2010). Our field data (e.g. Fig. 2a and Smith et al., 2007) constrain fault planes oriented at reactivation angles, θ_r, to σ'_1 of about 70° and 45° for weak and strong fault portions respectively (Fig. 10a). The reactivation, or re-shear condition (e.g. Sibson, 1985), results in a friction coefficient of 0.25 and 0.62 for the weak and strong fault portions respectively (Fig. 10b and friction data in Section 3.1). Under the boundary conditions described so far, during fault loading re-shear of the phyllosilicates occurs only for high values of fluid pressure, e.g. $\lambda=0.89$ (Fig. 10b), where λ is the ratio of fluid pressure to lithostatic load. The widespread hydrofractures system documented with the Zuccale fault core is in agreement with fluid overpressure during fault activity (Fig. 2b and Collettini et al., 2006; Smith et al., 2008). During frictional reactivation of the phyllosilicates, velocity- and shear-strengthening (Fig. 10c) make the condition for reactivation more severe (e.g. μ_s ~0.3, Fig. 10d); further reactivation can be achieved by either increases in fluid pressure (e.g. leftward shift of Mohr circle) or by a decrease of the minimum effective principal stress (Fig. 10d), that can eventually promote reactivation of faults in the stronger lenses (Fig. 10d). Several factors like crustal depth, differential stress, fluid pressure and cohesive strengthening of the fault zone (e.g. Fagereng et al., 2010; Muhuri et al., 2003; Streit and Cox, 2001; Tenthorey et al., 2003) influence the stress values of our mechanical analysis, however two main points can be highlighted. First, at crustal depth >4–5 km the reactivation of a weak fault that is oriented at high angles to the maximum compressive stress can be achieved only by fluid overpressure. Second, both along well oriented strong faults and misoriented weak faults (Fig. 10a), a small variation in differential stress or fluid pressure can trigger a switch from re-shear of strong to weak fault portions and vice versa (Fig. 10d).

Our results on the mixed-mode fault slip behavior are akin to findings from studies involving experiments on rock analogs (Niemeijer and Spiers, 2005) and field studies on the fault zone structure (Fagereng and Sibson, 2010; Faulkner et al., 2003). Here, by integrating field data on the fault zone structure with frictional properties of the fault rocks sheared under their in situ geometry, we provide further constraints for the mixed-mode fault slip behavior of crustal faults. We suggest that a better understanding of the complex fault slip behavior, documented in recent works using high-resolution seismological and GPS investigations, can be achieved by the integration of field studies of complex fault zone structures with the determination of the heterogeneous frictional properties of the fault rocks.

Acknowledgments

This research was supported by the ERC St. G. Nr. 259256 GLASS project and the U.S. National Science Foundation under grants NSF-EAR0950517 and NSF-EAR0911569 to C.J.M. A.N. is supported by the Netherlands Organisation Scientific Research (NWO) Veni grant Nr. 863.09.013. S.S. is supported by the ERC St. G. Nr. 205175, USEMS, project. We thank F. Trippetta and R.E. Holdsworth for discussion and S. Swavely for help in the laboratory. A. Fagereng, an anonymous reviewer and the Editor P. Shearer provided critical reviews, which significantly improved the paper.

Appendix A

Constitutive parameters for least-squares fit of the Dieterich Law. The standard deviation in a, b, and $a-b$ values is in the order of 10^{-4}, the standard deviation in d_c is generally less than 10% of d_c.

σ_n (MPa)	a	b	d_c	$a-b$	Vstep	Samples
10	0.007587	0.002796	23.51	0.004792	1–3	1f
10	0.007209	0.003178	32.59	0.004031	3–10	1f
10	0.007173	0.004995	112.32	0.002178	10–30	1f
10	0.008653	0.003948	73.42	0.004705	30–100	1f
10	0.010984	0.002248	26.21	0.008735	100–300	1f
20	0.006382	0.002449	19.52	0.003933	1–3	1f
20	0.006506	0.002454	31.55	0.004052	3–10	1f
20	0.007453	0.002683	34.27	0.004770	10–30	1f
20	0.008497	0.002254	40.48	0.006243	30–100	1f
20	0.010681	0.002234	31.84	0.008446	100–300	1f
35	0.006821	0.002018	7.57	0.004803	1–3	1f
35	0.006568	0.002027	21.6	0.004540	3–10	1f
35	0.008571	0.002015	31.12	0.006555	10–30	1f
35	0.007715	0.001776	33.61	0.005939	30–100	1f
35	0.009015	0.002010	26.15	0.007005	100–300	1f
50	0.006687	0.001614	8.95	0.005073	1–3	1f
50	0.006676	0.001900	16.04	0.004776	3–10	1f
50	0.006434	0.001745	21.78	0.004690	10–30	1f
50	0.007717	0.002294	31.89	0.005422	30–100	1f
50	0.008514	0.002768	29.05	0.005747	100–300	1f
75	0.006900	0.000635	42.64	0.006265	10–30	1f
75	0.007664	0.000482	14.04	0.007182	30–100	1f
75	0.008349	0.000610	35.17	0.007738	100–300	1f
100	0.006156	0.000568	19.79	0.005588	1–3	1f
100	0.005844	0.000363	17.36	0.005481	3–10	1f
100	0.006532	0.000691	46.96	0.005841	10–30	1f
100	0.007078	0.000589	41.04	0.006489	30–100	1f
100	0.008217	0.001414	50.45	0.006803	100–300	1f
150	0.006873	0.000587	56.36	0.006286	10–30	1f
150	0.007416	0.001283	37.78	0.006133	30–100	1f
150	0.008209	0.001449	43.57	0.006761	100–300	1f
10	0.006195	0.003882	29.93	0.002313	1–3	2f

Appendix A (*continued*)

σ_n (MPa)	a	b	d_c	$a-b$	Vstep	Samples
10	0.005206	0.003123	42363	0.002083	3–10	2f
10	0.006212	0.002860	10.44	0.003351	10–30	2f
10	0.006650	0.002584	23.44	0.004066	30–100	2f
10	0.006824	0.000556	30.49	0.006267	100–300	2f
20	0.006645	0.003013	16.64	0.003631	1–3	2f
20	0.006103	0.002137	20.63	0.003967	3–10	2f
20	0.006267	0.002308	26.85	0.003959	10–30	2f
20	0.006743	0.002233	22.71	0.004510	30–100	2f
20	0.006697	0.002028	16.87	0.004669	100–300	2f
35	0.006120	0.002007	24.84	0.004113	1–3	2f
35	0.005974	0.002210	37.03	0.003764	3–10	2f
35	0.006137	0.001700	35.52	0.004437	10–30	2f
35	0.006674	0.002226	41.43	0.004449	30–100	2f
35	0.007481	0.002251	22.71	0.005230	100–300	2f
50	0.006681	0.002409	17.19	0.004271	1–3	2f
50	0.006331	0.002285	25.08	0.004045	3–10	2f
50	0.006598	0.002308	21.73	0.004290	10–30	2f
50	0.006856	0.002206	26.21	0.004649	30–100	2f
50	0.006773	0.001691	38.61	0.005082	100–300	2f
75	0.007048	0.001709	9.15	0.005340	1–3	2f
75	0.006348	0.000840	11.15	0.005510	3–10	2f
75	0.007207	0.001350	12.94	0.005860	10–30	2f
75	0.006976	0.000449	11.83	0.006530	30–100	2f
75	0.008599	0.001910	10.36	0.006690	100–300	2f
100	0.005922	0.000722	18.44	0.005200	1–3	2f
100	0.007182	0.001603	16.67	0.005578	3–10	2f
100	0.007269	0.002100	13.3	0.005160	10–30	2f
100	0.006973	0.001532	24.1	0.005440	30–100	2f
100	0.008223	0.002516	15.55	0.005707	100–300	2f
150	0.006305	0.001317	12.65	0.004988	1–3	2f
150	0.006745	0.001492	15.94	0.005222	3–10	2f
150	0.006545	0.001595	24.95	0.004950	10–30	2f
150	0.007026	0.001804	32.01	0.005222	30–100	2f
150	0.007361	0.002117	45.14	0.005245	100–300	2f
10	0.006700	0.004500	21.32	0.002200	10–30	4p
10	0.005500	0.004800	70.12	0.000600	30–100	4p
10	0.004900	0.006200	119.71	−0.001200	100–300	4p
20	0.003900	0.005300	95.73	−0.001400	1–3	4p
20	0.003600	0.006100	110.72	−0.002500	3–10	4p
20	0.003900	0.006500	136.98	−0.002600	10–30	4p
20	0.004000	0.006600	137.95	−0.002500	30–100	4p
20	0.004700	0.008300	158.02	−0.003600	100–300	4p
35	0.003300	0.005600	104.17	−0.002300	1–3	4p
35	0.003600	0.005900	91.89	−0.002300	3–10	4p
35	0.004100	0.006400	97.06	−0.002300	10–30	4p
35	0.004200	0.006100	107.97	−0.001800	30–100	4p
35	0.004600	0.007400	127.11	−0.002800	100–300	4p
50	0.003200	0.006700	144.79	−0.003500	1–3	4p
50	0.003600	0.006600	145.7	−0.003000	3–10	4p
50	0.003900	0.006800	128.78	−0.002900	10–30	4p
50	0.004800	0.007000	113.63	−0.002100	30–100	4p
75	0.005700	0.003600	35.29	0.002100	1–3	4p
75	0.005700	0.003200	13.14	0.002500	3–10	4p
75	0.005600	0.003800	17.77	0.001800	10–30	4p
75	0.005200	0.004000	39.46	0.001200	30–100	4p
75	0.005000	0.005500	72.39	−0.000500	100–300	4p
100	0.005000	0.003900	17	0.001200	1–3	4p
100	0.004700	0.004100	28.94	0.000700	3–10	4p
100	0.004300	0.004100	49.12	0.000200	10–30	4p
100	0.004800	0.006500	82.94	−0.001700	100–300	4p
150	0.003800	0.002600	99.13	0.001200	1–3	4p
150	0.003800	0.003900	103.73	−0.000100	3–10	4p
150	0.004000	0.007000	170.84	−0.003000	10–30	4p
150	0.004600	0.007900	137.95	−0.003300	30–100	4p
150	0.005300	0.008700	117.9	−0.003400	100–300	4p

Appendix B

Constitutive parameters for least-squares fit of the Dieterich Law for samples 3 powders. The standard deviation in a, b_1, b_2 and $a-b$ is in the order of 10^{-4}, the standard deviation in d_{c1} and d_{c2} is generally less than 10% of the parameters.

σ_n (MPa)	a	b_1	d_{c1}	b_2	d_{c2}	a − b	V step	Samples
10	0.009816	0.004160	11.22	0.00279	60.07	0.002864	3–10	3p
10	0.010049	0.005420	12.58	0.00371	97.9	0.000920	10–30	3p
10	0.009854	0.005362	12.82	0.00482	143.13	−0.000330	30–100	3p
10	0.009720	0.005085	15.13	0.00488	153.73	−0.000240	100–300	3p
20	0.009134	0.005197	9.24	0.00199	65.58	0.001945	1–3	3p
20	0.009205	0.005277	9.23	0.00283	88.67	0.001101	3–10	3p
20	0.009824	0.004884	7.24	0.00397	81.35	0.000971	10–30	3p
20	0.009800	0.004961	8.32	0.00514	167.66	−0.000300	100–300	3p
35	0.008568	0.004418	10.46	0.00322	116.76	0.000932	3–10	3p
35	0.008890	0.004517	12.09	0.00397	159.85	0.000404	10–30	3p
35	0.009185	0.004101	10.52	0.00397	123.67	0.001114	30–100	3p
35	0.008881	0.004053	14.83	0.00847	422.8	−0.003650	100–300	3p
50	0.007611	0.003754	14.3	0.00308	138.35	0.000780	1–3	3p
50	0.007741	0.003481	16.89	0.00709	357.49	−0.002830	3–10	3p
50	0.008400	0.003388	15.96	0.00699	267	−0.001980	10–30	3p
50	0.009335	0.003649	16.98	0.00987	352.45	−0.004190	30–100	3p
50	0.008646	0.003197	16.93	0.01021	285.22	−0.004760	100–300	3p
75	0.005676	0.003612	35.29	modeling with only b		0.002065	1–3	3p
75	0.005738	0.003191	13.14	modeling with only b		0.002548	3–10	3p
75	0.005632	0.003792	17.77	modeling with only b		0.00184	10–30	3p
75	0.007936	0.003521	14.71	0.00396	157.16	0.000454	30–100	3p
75	0.008278	0.004158	16.85	0.00874	321.26	−0.004620	100–300	3p
100	0.007390	0.002500	14.59	0.00256	50.06	0.002334	30–100	3p
100	0.008373	0.003847	15.18	0.00379	138	0.000732	100–300	3p
150	0.006379	0.002238	21.48	0.00194	243.32	0.002198	3–10	3p
150	0.006442	0.002548	25.1	0.00440	207.73	−0.000510	10–30	3p
150	0.006938	0.003211	31.44	0.00523	223.99	−0.001510	30–100	3p
150	0.008048	0.003875	24.1	0.00691	173.48	−0.002740	100–300	3p

References

Beeler, N.M., Tullis, T.E., Blanpied, M.L., Weeks, J.D., 1996. Frictional behaviour of large displacement experimental faults. J. Geophys. Res. 101, 8697–8715.

Blanpied, M.L., Marone, C.J., Lockner, D.A., Byerlee, J.D., King, D.P., 1998. Quantitative measure of the variation in fault rheology due to fluid-rock interactions. J. Geophys. Res. 103, 9691–9712.

Boettcher, M.S., McGarr, A., Johnston, M., 2009. Extension of Gutenberg-Richter distribution to Mw −1.3, no lower limit in sight. Geophys. Res. Lett. 36, L10307. doi:10.1029/2009GL038080.

Bos, B., Spiers, C.J., 2002. Frictional-viscous flow of phyllosilicate bearing fault rock: microphysical model and implications for crustal strength profiles. J. Geophys. Res. 107 (B2), 2028. doi:10.1029/2001JB000301.

Boutareaud, S., Calugaru, D.G., Han, R., Fabbri, O., Mizoguchi, K., Tsutsumi, A., Shimamoto, T., 2008. Clay-clast aggregates: a new 0 structural evidence for seismic sliding? Geophys. Res. Lett. 35, L05302. doi:10.1029/2007GL032554.

Brace, W.F., Kohlstedt, D.L., 1980. Limits on lithospheric stress imposed by laboratory experiments. J. Geophys. Res. 85, 6348–6352.

Byerlee, J.D., 1978. Friction of rocks. Friction of rocks. Pure Appl. Geophys. 116, 615–629.

Carpenter, B.M., Marone, C., Saffer, D.M., 2011. Weakness of the San Andreas Fault revealed by samples from the active fault zone. Nat. Geosci. 4, 251–254. doi:10.1038/ngeo1089.

Cashman, S.M., Baldwin, J.N., Casman, K.V., Swanson, K., Crawford, R., 2007. Microstructures developed by coseismic and aseismic faulting in near-surface sediments, San Andreas fault, California. Geology 35, 611–614.

Chen, K.H., Rau, R.J., Hu, J.C., 2009. Variability of repeating earthquake behaviour along the Longitudinal Valley fault zone of eastern Taiwan Source. J. Geophys. Res. 114, B05306. doi:10.1029/2007JB005518.

Chester, F.M., 1995. A rheologic model for wet crust applied to strike-slip faults. J. Geophys. Res. 100, 13033–13044.

Chester, F.M., Chester, J.S., 1998. Ultracataclasite structure and friction processes of the Punchbowl fault, San Andreas system, California. Tectonophysics 295, 199–221.

Chiaraluce, L., Chiarabba, C., Collettini, C., Piccinini, D., Cocco, M., 2007. Architecture and mechanics of an active low angle normal fault: the Alto Tiberina fault (northern Apennines, Italy) case study. J. Geophys. Res. doi:10.1029/2007JB005015.

Collettini, C., Holdsworth, R.E., 2004. Fault zone weakening processes along low-angle normal faults: insights from the Zuccale Fault, Isle of Elba, Italy. J. Geol. Soc. 161, 1039–1051.

Collettini, C., Trippetta, F., 2007. A slip tendency analysis to test mechanical and structural control on aftershock rupture planes. EPSL 255, 402–413.

Collettini, C., De Paola, N., Goulty, N.R., 2006. Switches in the minimum compressive stress direction induced by overpressure beneath a low-permeability fault zone. Terra Nova 18, 224–231.

Collettini, C., Viti, C., Smith, S.A.F., Holdsworth, R.E., 2009a. The development of interconnected talc networks and weakening of continental low-angle normal faults. Geology 37, 567–570.

Collettini, C., Niemeijer, A., Viti, C., Marone, C., 2009b. Fault zone fabric and fault weakness. Nature 462, 907–910.

Cowan, D.S., Cladouhos, T.T., Morgan, J., 2003. Structural geology and kinematic history of rocks formed along low-angle normal faults, Death Valley, California. Geol. Soc. Am. Bull. 115, 1230–1248.

Di Toro, G., Han, R., Hirose, T., De Paola, N., Nielsen, S., Mizoguchi, K., Cocco, M., Shimamoto, T., 2011. Fault lubrication during earthqakes. Nature 471, 494–497.

Dieterich, J.H., 1979. Modelling of rock friction: 1. Experimental results and constitutive equations. J. Geophys. Res. 84, 2161–2168.

Dieterich, J.H., Kilgore, B., 1994. Direct observation of frictional contacts: new insights for state dependent properties. Pure Appl. Geophys. 143, 283–302.

Fagereng, A., 2011. Frequency-size distribution of competent lenses in a block-in-matrix mélange: imposed length scales of brittle deformation? J. Geophys. Res. 116, B05302. doi:10.1029/2010JB007775.

Fagereng, A., Sibson, R.H., 2010. Melange rheology and seismic style. Geology 38, 751–754.

Fagereng, A., Remitti, F., Sibson, R.H., 2010. Shear veins observed within anisotropic fabric at high angles to the maximum compressive stress.

Faulkner, D.R., Lewis, A.C., Rutter, E.H., 2003. On the internal structure and mechanics of large strike-slip faults: field observations from the Carboneras fault, southeastern Spain. Tectonophysics 367, 235–251.

Goodwin, L.B., Tikoff, B., 2002. Competency contrast, kinematics and the development of foliations and lineations in the crust. J. Struct. Geol. 24, 1065–1085.

Gratier, J.P., Guiguet, R., Renard, F., Jenatton, L., Bernard, D., 2009. A pressure solution creep law for quartz from indentation experiments. J. Geophys. Res. Solid Earth 114.

Gueydan, F., Leroy, Y., Jolivet, L., 2003. Mechanics of low-angle extensional shear zones at the brittle–ductile transition. J. Geophys. Res. 109, 1–18.

Holdsworth, R.E., 2004. Weak faults—rotten cores. Science 303, 181–182.

Hreinsdottir, S., Bennett, R.A., 2009. Active aseismic creep on the Alto Tiberina low-angle normal fault, Italy. Geology 37, 683–686.

Ikari, M.G., Marone, C., Saffer, D.M., 2009. Frictional and hydrologic properties of clay-rich fault gouge. J. Geophys. Res. 114, B05409.

Ikari, M.G., Neimeijer, A.R., Marone, C., 2011. The Role of Fault Zone Fabric and Lithification State on Frictional Strength, Constitutive Behavior and Deformation Microstructure. J. Geophys. Res. 109, 25 pp.

Ito, Y., Obara, K., 2006. Dynamic deformation of the accretionary prism excites very low frequency earthquakes. Geophys. Res. Lett. 33, L02311. doi:10.1029/2005GL025270.

Jefferies, S.P., Holdsworth, R.E., Shimamoto, T., Takagi, H., Lloyd, G.E., 2006. The formation and significance of foliated cataclasite and gouge in the cores of crustal-scale

faults: examples from the Median Tectonic Line, Japan. J. Geophys. Res. 111, B12303. doi:10.1029/2005JB004205.
King, C.Y., Nason, R.D., Tocher, D., 1973. Kinematics of fault creep, a discussion on the measurement and interpretation of changes of strain in the earth. Philos. Trans. R. Soc. London, A 274 (1239), 355.
Kitajima, H., Chester, C.J., Chester, F.M., Frederick, T., Shimamoto, T., 2010. High-speed friction of disaggregated ultracataclasite in rotary shear: characterization of frictional heating, mechanical behavior, and microstructure evolution. J. Geophys. Res. 115, B08408.
Lisle, R.J., Srivastava, D.C., 2004. Test of the frictional reactivation theory for faults and validity of fault–slip analysis. Geology 32, 569–572.
Logan, J.M., 1978. Creep, stable sliding, and premonitory slip. Pure Appl. Geophys. 116, 773–789.
Marone, C., 1998. Laboratory-derived friction laws and their application to seismic faulting. Annu. Rev. Earth Planet. Sci. 26, 643–696.
Marone, C., Kilgore, B., 1993. Scaling of the critical slip distance for seismic faulting with shear strain in fault zones. Nature 362, 618–621.
Marone, C., Scholz, C.H., 1988. The depth of seismic faulting and the upper transition from stable to unstable slip regimes. Geophys. Res. Lett. 15, 621–624.
Moore, D.E., Lockner, D.A., 2007. Friction of the smectite clay montmorillonite: a review and interpretation of data. In: Dixon, T.H., Moore, J.C. (Eds.), The Seismogenic Zone of Subduction Thrust Faults: MARGINS Theoretical and Experimental Earth Science Ser., 2, pp. 317–345.
Moore, D.E., Lockner, D.A., 2008. Talc friction in the temperature range 25°–400 °C: relevance for fault-zone weakening. Tectonophysics 449, 120–132. doi:10.1016/j.tecto.2007.11.039.
Moore, D.E., Rymer, M., 2007. Talc-bearing serpentinites and the creeping section of the San Andreas fault. Nature 448, 795–797. doi:10.1038/nature06064.
Morris, A., Ferril, A., Henderson, D.B., 1996. Slip tendency analysis and fault reactivation. Geology 24, 275–278.
Muhuri, S.K., Dewers, T.A., Scott, T.E., Reches, Z., 2003. Interseismic fault strengthening and earthquake-slip stability: friction of cohesion? Geology 31, 881–884.
Niemeijer, C. Marone, Elsworth, D., 2010. Fabric induced weakness of tectonic faults. Geophys. Res. Lett. 37, L03304. doi:10.1029/2009GL041689.
Niemeijer, A.R., Spiers, C.J., 2005. Influence of phyllosilicates on fault strength in the brittle–ductile transition: insights from rock analogue experiments. J. Geol. Soc. London Spec. Pub. 245, 303–327.
Niemeijer, A.R., Spiers, C.J., 2007. A microphysical model for strong velocity-weakening in phyllosilicate-bearing fault gouges. J. Geophys. Res. 112, B10405. doi:10.1029/2007JB005008.
Niemeijer, A., Elsworth, D., Marone, C., 2009. Significant effect of grain size distribution on compaction rates in granular aggregates. EPSL. doi:10.1016/j.epsl.2009.04.041.
Niemeijer, A., Collettini, C., Smith, S.A.F., Spiers, C.J., 2011. Frictional properties of Zuccale Fault rocks from room temperature to in-situ conditions: results from high strain rotary shear experiments. Deformation Rheology and Tectonics conference (abstract).
Peng, Z., Gomberg, J., 2010. An integrated perspective of the continuum between earthquakes and slow-slip phenomena. Nat. Geosci. 3, 599–607.
Perfettini, H., et al., 2010. Seismic and aseismic slip on the central Peru megathrust. Nature 465, 78–81.
Power, W.L., Tullis, T.E., 1989. The relationship between slickenside surfaces in fine-grained quartz and the seismic cycle. JSG 11, 879–893.
Reinen, L.A., Weeks, J.D., 1993. Determination of rock friction constitutive parameters using an iterative least-squares inversion method. J. Geophys. Res. 98, 15937–15950.
Rubinstein, J.L., Shelly, D.R., Ellsworth, W.L., 2010. Non-volcanic Tremor: A Window into the Roots of Fault Zones. In: Cloetingh, S., Negendank, J. (Eds.), New Frontiers in Integrated Solid Earth Sciences, pp. 287–314.
Ruina, A., 1983. Slip instability and state variable friction laws. J. Geophys. Res. 88, 10359–10370.
Saffer, D.M., Marone, C., 2003. Comparison of smectite- and illite rich gouge frictional properties: application to the up-did limit of the seismogenic zone along subduction mega-thrusts. Earth Planet. Sci. Lett. 215, 219–235.
Scholz, C.H., 1998. Earthquakes and friction laws. Nature 391, 37–42.
Scholz, C.H., 2000. Evidence for a strong San Andreas fault. Geology 28, 163–166.
Sibson, R.H., 1985. A note on fault reactivation. J. Struct. Geol. 7, 751–754.
Sibson, R.H., 2003. Thickness of the seismic slip zone. Bull. Seismol. Soc. Am. 93, 1169–1178.
Smith, S.A.F., Holdsworth, R.E., Collettini, C., 2007. The role of footwall structures in the evolution of low-angle normal faults. J. Geol. Soc. 164, 1187–1191.
Smith, S.A.F., Collettini, C., Holdsworth, R.E., 2008. Recognising the seismic cycle along ancient faults: CO_2-induced fluidization of breccias in the footwall of a sealing low-angle normal fault. J. Struct. Geol. 20, 134–146.
Smith, S.A.F., Holdsworth, R.E., Collettini, C., Pearce, M., 2011. The microstructural character and mechanical significance of fault rocks associated with a continental low-angle normal fault: the Zuccale fault, Elba Island, Italy (Accepted for Publication) Journal of the Geological Society Special Publications: Geology of the Earthquake Source (A Volume in Honor of Rick Sibson).
Streit, J.E., Cox, S.F., 2001. Fluid pressure at hypocenters of moderate to large earthquakes. J. Geophys. Res. 106, 2235–2243.
Tenthorey, E., Cox, S.F., Todd, H.F., 2003. Evolution of strength recovery and permeability during fluid-rock reaction in experimental fault zones. Earth Planet. Sci. Lett. 206 (1–2), 161–172. doi:10.1016/S0012- 1117821X(02)01082-8.
Vannucchi, P., Remitti, F., Bettelli, G., 2007. Geological record of fluid flow and seismogenesis along an erosive subducting plate boundary. Nature 451, 699–703.
Verberne, B.A., He, C., Spiers, C.J., 2010. Frictional properties of sedimentary rocks and natural fault gouge from the Longmen Shan Fault Zone, Sichuan, China. BSSA 100 (5B), 2767–2790. doi:10.1785/0120090287.
Waldhauser, F., Ellsworth, W.L., Schaff, D.P., Cole, A., 2004. Streaks, multiplets, and holes: high-resolution spatiotemporal behaviour of Parkfield seismicity. Geophys. Res. Lett. 31, L18608. doi:10.1029/2004GL020649.
Wibberley, C.A.J., Shimamoto, T., 2003. Internal structure and permeability of major slip fault zones: the median tectonic line in Mie prefecture, southwest Japan. J. Struct. Geol. 25, 59–78. doi:10.1016/S0191-8141(02)00014-7.
Wintsch, R.P., Christoffersen, R., Kronenberg, A.K., 1995. Fluid-rock reaction weakening of fault zones. J. Geophys. Res. 100, 13021–13032.
Zoback, M., Hickman, S., Ellsworth, W., 2010. Scientific drilling into the San Andreas fault zone. Eos 91, 197–204.